Empirical Dynamic Modeling Reveals Complexity of Methane Fluxes in a Temperate Salt Marsh

Authors:

Andrew C Hill[1], Karina Schafer[2], Inke Forbrich[3,4], Rodrigo Vargas[1*]

Affiliations:

[1]University of Delaware, Department of Plant & Soil Sciences, 531 South College Ave., 152 Townsend Hall, Newark, DE 19716, USA

[2]Rutgers University, Department of Earth and Environmental Sciences, 101 Warren St, Smith Hall, Newark, NJ 07102, USA

[3]Marine Biological Laboratory, The Ecosystems Center, 7 MBL Street, Woods Hole, MA 02543, USA

[4]Department of Environmental Sciences, University of Toledo, 2801 W. Bancroft Street, Toledo, OH 43606, USA

*Corresponding author: Rodrigo Vargas (rvargas@udel.edu)

Abstract

Methane dynamics within salt marshes are complex because vegetation types, temperature, oscillating water levels, and changes in salinity and redox conditions influence CH4 production and emission. These non-linear and complex interactions among variables affect the traditionally expected functional relationships and present challenges for interpretation and developing process-based models. We employ empirical dynamic modeling (EDM) and convergent cross mapping (CCM) as a novel approach for characterizing seasonal/multiday and diurnal CH_4 dynamics by identifying causal variables, lags, and interconnections among multiple biophysical variables within a temperate salt marsh using five years of eddy covariance data. EDM/CCM is a nonparametric approach capable of quantifying the coupling between variables while determining time scales where variable interactions are most relevant. We found that gross primary productivity, tidal creek dissolved oxygen, and temperature were important for seasonal/multiday dynamics (rho=0.73-0.80), while water level was most important for diurnal dynamics during both the growing and dormancy phenoperiods (rho=0.72 and 0.56, respectively). Lags for top causal variables (gross primary productivity, tidal creek dissolved oxygen, temperature, water level) occurred between 1-5 weeks at the seasonal scale and 1-24 hours at the diurnal scale. The EDM had high prediction capabilities for intra-/inter-seasonal patterns and annual CH_4 sums but with limitations to represent large infrequent fluxes. Results highlight the importance of non-linearity, causal drivers, lag times, and interconnections among multiple biophysical variables that regulate CH_4 fluxes in tidal wetlands. This study presents a new dimension for analyzing CH_4 fluxes, which will prove helpful to test current paradigms in wetlands and other ecosystems.

Keywords: Methane flux, Saltmarsh, Nonlinear dynamics, Methane prediction, Empirical dynamic modeling, Tidal wetland

Plain Language Summary

The movement of methane gas in salt marshes is complex and influenced by various factors such as plant types, temperature, water level, and changes in water salinity and oxygen levels. These factors interact in intricate ways, making it difficult to predict the outcome of methane production and movement. We applied a new method of studying methane dynamics using Empirical Dynamic Modeling (EDM) and Convergent Cross Mapping (CCM). After analyzing five years of ecosystem-scale measurements of methane fluxes, we show that the amount of oxygen in the water, the temperature, and the amount of light received by plants are crucial for understanding regulating methane fluxes within days and across seasons. The interconnections among these variables are complex, and methane fluxes may have delayed responses, which highlight the importance of these interactions. This research improves our comprehension of how environmental factors interact to affect methane fluxes in wetlands.

Key points

- Methane dynamics in salt marshes are complex and influenced by multiple variables.
- Empirical dynamic modeling (EDM) and convergent cross mapping (CCM) are novel approaches to characterizing CH_4 dynamics.
- Results highlight non-linearity, causal drivers, lag times, and interconnections among multiple biophysical variables for CH_4 dynamics.

1. Introduction

Methane (CH_4) is the second most potent greenhouse gas and a crucial atmospheric trace gas with a warming potential 25-38 times greater than carbon dioxide (CO_2) (Wuebbles and Hayhoe 2002, Bridgham et al. 2013, Neubauer and Megonigal 2019). Following a largely unreconciled plateau during a stabilized phase from 2000-2006, there has been a steady global rise, with wetlands likely responsible for most natural contributions (Jackson et al. 2020). While there is evidence that this increase is the result of both anthropogenic and biogenic emissions (Stavert et al. 2022), there is no easy mitigation option for biogenic sources, and climate change could increase these emissions resulting in positive feedback for the global carbon cycle (Dean et al. 2018, Zhang et al. 2017). This is especially important for coastal wetlands where warming and sea level rise are expected to impact CH_4 fluxes directly through changes in microbial metabolism (Yvon-Durocher et al. 2014), and indirectly from effects on co-dependent factors such as plant productivity (GPP) and sediment redox conditions (Strom et al. 2015, Liu et al. 2019, Seyfferth et al. 2020).

Mechanisms driving CH_4 fluxes are complex within coastal wetlands with many potential regulators (Huertas et al. 2019, Vázquez-Lule and Vargas 2021). Water level and waterlogged conditions have been identified as a substantial control for methanogenesis (Li 2007), but these ecosystems have been considered low CH_4 emitters despite prevailing anoxic conditions (Conrad 2020, Bartlett et al. 1987, Wang, Zeng and Patrick 1996, Borges and Abril 2011). This paradigm relies on the idea that acetoclastic or hydrogenotrophic methanogenesis are the dominant biogeochemical pathways and prevailing sulfate-reducing bacteria outcompete methanogens (Poffenbarger, Needelman, and Megonigal 2011). However, new evidence indicates coastal wetlands could have high CH_4 fluxes where other biogeochemical pathways, such as methylotrophic methanogenesis, play essential roles (Al-Haj and Fulweiler 2020, Seyfferth et al. 2020, Conrad 2020). In addition, it has been recognized that multiple environmental factors (e.g., water level, temperature, GPP, salinity) regulate CH_4 fluxes at different temporal scales with potential nonlinear interactions (Huertas et al. 2019, Reid et al. 2013, Li et al. 2018). Consequently, it is

imperative that we accurately understand how biophysical controls regulate CH_4 fluxes in coastal wetlands to better understand ecosystem response to environmental change.

Our past knowledge of CH_4 dynamics in tidal wetlands has vastly relied on chamber-based manual measurements. This information has influenced the development of most functional relationships (e.g., salinity thresholds or temperature dependency) and, subsequently their incorporation into models used to predict CH_4 fluxes. However, chambers often face logistical challenges and are sporadic in time and space, restricting our understanding by delivering limited or incomplete information (Hill and Vargas 2022, Kim 2007, Yang et al. 2021). Technological advances have allowed us to collect higher frequency CH_4 fluxes at the ecosystem scale using the eddy covariance technique (EC) (Morin 2019, Baldocchi 2003). This data can be leveraged to explore relationships in greater detail, providing a wealth of information regarding the dynamics of driving mechanisms. Previous studies have analyzed how biophysical variables regulate ecosystem-scale CH_4 fluxes in salt marshes (Vázquez-Lule and Vargas 2021, Hill and Vargas 2022, Huertas et al. 2019, Li et al. 2018, Reid et al. 2013). Other studies outside salt marshes have used machine learning techniques (Rey-Sanchez et al. 2018, Zaki and Abdul-Aziz 2022) or time series analysis and information theory to identify the dominant controls of ecosystem-scale CH_4 fluxes (Knox et al. 2021, Sturtevant et al. 2016). Together, these studies provide insights into the complex mechanisms and hint that nonlinear dynamics may be more relevant for explaining ecosystem-scale CH_4 fluxes. Therefore, there is a need to identify potential lags, interactions, and interconnections to provide insights about causality and biogeochemical mechanisms controlling CH_4 fluxes across wetland types.

The complexity of CH_4 dynamics in coastal wetlands results from interacting variables that cannot be readily isolated to identify independent functional relationships (Morin 2019; Vazquez-Lule and Vargas 2021). This complexity also brings an opportunity to test alternative methods for data analysis. As a novel approach, we employed a form of nonlinear state space reconstruction referred to as empirical dynamic modeling (EDM; Sugihara and May 1990, Sugihara et al. 2012). We propose EDM as an alternative to techniques such as Granger Causality, wavelets, and information theory to unravel

112 complex non-linear CH_4 dynamics using the wealth of information from continuous time series generated
113 from EC data (Schafer, Tripathee et al. 2014, Sturtevant, Ruddell et al. 2016, Li, Dai et al. 2018, Knox,
114 Bansal et al. 2021). This method falls within nonlinear dynamical systems but differs from other widely
115 used prediction-based methods, such as Granger Causality, which holds the criteria of separability
116 (Granger 1969) and may be less effective in identifying weak-moderate couplings (Guo et al. 2022). The
117 premise of EDM relies upon a simplex projection algorithm, the nearest neighbor forecasting method, that
118 tracks the evolution of nearby points within a lagged coordinate state space reconstruction or embedding
119 (Hsieh et al. 2005). In other words, simplex projection attempts to predict future values based on when
120 similar patterns were observed in the past, with more similar past patterns assigned a higher weight for
121 calculating the mean location of the predicted point (Petchey, 2016). In this study, we implement a form
122 of EDM known as convergent cross mapping (CCM) as a novel approach and alternative technique to
123 disentangling CH_4 dynamics with EC data within a temperate coastal salt marsh (Munch, Rogers, and
124 Sugihara 2022). We chose the CCM approach because it can describe the complex interrelations in a
125 dynamic ecological system where dependencies cannot be evaluated independently.
126 Here we examine five years of ecosystem-scale CH_4 fluxes using the EC technique and CCM to
127 study seasonal and diurnal CH_4 fluxes (i.e., dependent variable) by quantifying the coupling between
128 independent variables (i.e., predictors) while considering time lags and interconnections. Briefly, CCM
129 uses state space reconstruction methods that allow us to analyze how variables interact and change with
130 the flow of time by examining past variable states to determine if similar dynamics are embedded in the
131 presently observed target variable (i.e., CH_4). This method is appropriate for informing causality within
132 complex nonlinear systems where lags or inconsistent relationships commonly manifest (McGowan et al.
133 2017), and works within the time domain, which is fundamentally different from wavelet analysis which
134 focuses on the frequency domain (Vargas et al. 2010). CCM can also identify complex interactions where
135 the indirect effect of one variable is relevant via a second variable that directly influences the dependent
136 variable. Consequently, CCM can provide interpretable empirical models that can be used to develop
137 predictions for gap filling of data or forecasting applications. Because CH_4 dynamics exhibit complex

patterns generated by multiple interactions, we propose that CCM is best suited to identify the nonlinearities and potential causal relationships that regulate CH_4 dynamics in wetlands and other terrestrial ecosystems.

2. Materials and Methods

2.1 Study Site

This study was performed at the St. Jones Reserve as part of the Delaware National Estuarine Research Reserve System (DNERR). The site is representative of a mid-Atlantic salt marsh with a mean elevation of 0.60 ± 0.26 m relative to the NAVD88 datum (McKenna et al., 2018), yet is still influenced by semi-diurnal tidal activity and site hydrology (i.e., riverine and groundwater flows). Vegetation is dominated by a monoculture of short-form *S. alterniflora* (~66%). The remaining cover (~33%) is associated with tall *S. alterniflora, S. cynosuroides, and P. australis,* which flank tidal creeks, and *S. patens* and *P. australis* along the upland terminus (Vázquez-Lule and Vargas 2021). Previous studies conducted in this wetland suggest the presence of methylotrophic methanogenesis responsible for very high CH_4 concentrations (>200 μM) within the sediments (Seyferth et al. 2020) but with low CH_4 sediment-atmosphere emissions (Capooci and Vargas 2022) These findings challenge the current paradigm that low methanogenesis is expected in tidal wetlands and consequently new approaches are needed to identify the complexity of the underlying biophysical drivers.

2.2 Data Acquisition

2.2.1 Eddy Covariance Measurements

The eddy covariance (EC) technique was used to measure the ecosystem-scale net exchange of CH_4 with an open path near-infrared gas analyzer (Li-7700, Licor, Lincoln, NE, USA) and ecosystem-scale net exchange of CO_2 (NEE) with an enclosed path infrared gas analyzer (Li-7200, Licor, Lincoln, NE, USA), and wind components with a 3D sonic anemometer (Gill Windmaster Pro, Gill Instruments,

Lymington, UK) recording measurements at 10 Hz. Preprocessing was completed in Eddy Pro (version 7.0.6), which consisted of time lag compensations, double coordinate rotation of wind components, and Reynolds block averaging to calculate 30-minute fluxes of CH_4 and CO_2. Expanded preprocessing and tower set-up descriptions can be found elsewhere (Vázquez-Lule and Vargas 2021, Hill and Vargas 2022). During post-processing, several standardized Ameriflux QA/QC procedures were applied, including removing values flagged for low quality during pre-processing, calculating nighttime storage fluxes determined by Eddy Pro, and range filtering of CO_2 to remove outliers falling beyond +/- 50 umol m^{-2} s^{-1}. A range filter was not applied to CH_4 data as spikes since ebullition could occur, and the goal was to incorporate all CH_4 dynamics within the 30-minute block averaging period. In addition, we used an optimal friction velocity (u*) threshold of 0.069 m s^{-1} to remove low turbulence conditions and applied a fetch/footprint filter to exclude fluxes originating from forested regions beyond the marsh terminus (Vázquez-Lule and Vargas 2021).

Data gaps occurring in NEE were filled using marginal distribution sampling (MDS) with customized site variables consisting of energy fluxes (sensible and latent heat; H and LE), radiation, air temperature (Tair), soil temperature (Tsoil), relative humidity (RH) and vapor pressure deficit (VPD) (Vázquez-Lule and Vargas 2021). Partitioning of NEE into component fluxes of gross primary productivity (GPP) was completed with the REddyProc R package (Reichstein et al., 2005; Wutzler et al., 2018) based on the standard nighttime method (Reichstein et al., 2005). To fill gaps in CH_4 fluxes, we applied a random forest technique with the Caret R package and used a full suite of relevant site variables (Fig. S2) (Kim et al., 2020; Kuhn et al. 2016). This method was selected because it is less biased when identifying predictors of CH_4 flux and because CCM requires continuous gap-filled data (Kim et al., 2020; Chang, Ushio, and Hsieh 2017).

2.2.2 Meteorology and Water Quality Measurements

Meteorological variables included air temperature (Tair) and relative humidity (RH, HC2-S3, Campbell Scientific, Logan, UT), precipitation (Precip) (TE 525, Tipping Bucket Rain Gauge, Campbell

Scientific, Logan, UT), photosynthetically active radiation (PAR) (SQ-110, quantum sensor, Apogee, Logan, UT), air pressure (Patm) (CS-106, Vaisala, Vantaa, Finland) and wind speed (WSpd) (05103-L Wind Monitor, Campbell Scientific, Logan, UT). VPD was calculated using Tair and RH based on the Tetens formula (Murray 1967). Water quality data were collected from the tidal creek adjacent to the EC tower using a YSI EXO2 sonde outfitted with EXO sensors. Measured variables included water temperature (Twater), water level (Level), salinity (Sal), and dissolved oxygen (DO). Meteorological and water quality data were averaged for 30 minutes to align with flux data. Minor gaps in meteorological data were filled using available on-site sensors. Gaps in water quality data, which mainly occurred during the dormancy phenoperiod, were filled using empirical relationships from another YSI EXO2 sonde located approximately 2.0 km upstream within the St. Jones River, which shares connectivity to the tidal channel. Meteorological and water quality data were collected under the National Estuarine Research Reserve (NERR) Centralized Data Management Protocol (Kennish, 2019) and can be accessed from the NERR System Centralized Data Management Office (NERR CDMO; station: delsjmet-p).

2.3 Data Selection and Phenology

For examining seasonal CH_4 dynamics, we selected five years spanning 2017-2021 to calculate daily means of non-gap-filled observations. This period was chosen as all years contained minimal continuous gaps (<30 days). To examine diurnal dynamics, we used data only from 2020-21, the period with the most complete record (i.e., containing 15% of data gaps) and when no substantial water surges or storm events occurred. To delineate these periods, we determined phenology dates with the Phenopix R package using the greenness chromatic coordinate (GCC) from a site phenocam (Filippa et al. 2016, Hill, Vázquez-Lule and Vargas 2021). Season start and end dates were calculated based on the upturn and recession dates of the annual GCC curve from daily midday images (Gu et al., 2009). To avoid an artifact of calendar years that would result in discontinuous time series for dormancy data, we included the tail end of 2020 and excluded the tail end of 2021.

2.4 Convergent Cross Mapping

While previous studies have described in detail the methodology behind CCM (Ushio and Kawatsu 2020, Sugihara and May 1990, Sugihara et al. 2012, Chang, Ushio and Hsieh 2017, Tsonis et al. 2018, Wang et al. 2018), we provide a brief overview of the implementation of CCM and how we interpreted results as they pertain to the goals of the current study (Fig. S1). All CCM analysis was completed within the rEDM R package (Ye et al. 2016).

To evaluate the causality between variables, we applied CCM between CH_4 and all independent variables via the function *CCM* (Ye et al. 2016). The CCM function is essentially a wrapper for the simplex algorithm but accesses the level improvement in nearest neighbor predictions within the state space as the data sample size increases. Specifically, this tests if lags of a predictor variable can be used to predict a target variable (e.g., does GPP have a causal relationship with CH_4) (Tsonis et al. 2018, Schiecke et al. 2015, Sugihara et al. 2012). It is a standard procedure also to test the opposite cross mapping (i.e., does CH_4 have a causal relationship with GPP). In a dynamic system, information about the causal variable becomes embedded within the target variable (i.e., information about past causal variables is observed in the present target variable). CCM is carried out using successively larger data samples or libraries. Predictive skill is evaluated with the output parameter rho (the overall skill of the cross-mapping) and is expected to increase with increasing library (data) size (i.e., convergence) subsampled randomly from the main dataset as the first criterion for causation (Chang et al. 2017). The predictive skill at maximum library size (the complete data set) is further compared to results generated from a surrogate dataset containing a preserved seasonal phase amplitude with the original data randomized in time. Cross mappings need a higher final predictive skill than the final surrogate predictive skill as a second criterion for causation via this significance test (Tsonis et al. 2018). Aside from verifying convergence with increasing data libraries, all figures in this study present results from the full data library size for both surrogate and real data, representing 5 complete years of data.

Two steps are applied before CCM, which provide information about the time series of interest (CH_4) (Li et al. 2021). The initial step is determining the embedding dimension (e) via the function *EmbedDimension,* which iteratively takes successively longer lags of a set time period defined by the parameter Tau (T). For this study, we set T to the default value of T=1 to represent one day for seasonal analyses and one hour for diurnal analyses. The lagged time series are then projected into an e-dimensional state space, forming a shadow manifold or state space projection (Ye et al. 2016) (Fig. S3). The resulting manifolds are then projected back onto a coordinate axis with the best embedding dimension resulting in a nearly 1:1 mapping of the original time series (Fig. S4). The number of dimensions (e) required to recreate the original time series is both a metric of complexity and an a priori requirement for CCM. The second step is confirming nonlinear dynamics by constructing sequential locally weighted global linear maps (S-map). S-maps are like nearest neighbor predictions from the simplex algorithm, but instead of considering the average localization of the nearest neighbors, all neighboring points are regarded with more weight given to closer neighbors through an exponential localization function (Sugihara et al. 1994). This is done via the function *PredictNonlinear,* which determines if predictions made by S-maps depend on the local state of the variable being predicted as defined by the parameter theta (Θ) in a locally weighted linear regression function. If predictive skill increases at Θ>0, we assume that predictions are highly dependent on ecosystem state space (i.e., variable interactions change with time or under specific conditions) and the hallmark of a nonlinear dynamical system (Chang et al. 2017).

We applied year-round daily data for seasonal dynamics with a minimum library size of n=15 days and a maximum of n=1,800 days. For diurnal dynamics, hourly data was used from the selected growing and dormancy phenoperiods using a minimum library size of n=15 hours and a maximum of n=2,900 and n=2,700 hours, respectively. CCM was carried out using 100 sample runs with the default time period for lags set to 1 unit (Tp=1 day or hour). The execution radius, which ignores nearest neighbors within the state space projection, was set at one day or 24 hours to help eliminate influence from temporal autocorrelation. To generate surrogate datasets, the original data was randomized in time

with the seasonal phase amplitude preserved for daily data by setting the method to 'seasonal'. For hourly data, the method was set to 'random' (Deyle et al. 2016).

2.5 Model Interpretation with Extended CCM and Causal Network Maps

Conventional CCM provides a robust means of identifying causality between variable pairs, yet it fails to capture the optimal time period of the causal influence. Extended CCM is a computationally intensive technique that involves applying CCM iteratively across multiple time period lags to determine time periods where cross-mapping skills are maximized. The procedure is also used to help resolve issues of generalized synchrony where cross-mapping is significant in both directions (i.e., Tair causality on CH_4 and CH_4 causality on Tair) (Example: Fig. S7 panel C) as the most probable causal relationship will generally have a maximum predictive skill which peaks within the negative time domain (i.e., negative lags) (Fig. S8) (Ye et al. 2015b). Causal influence can occur synchronously, over a day, several hours, or an extended period, several consecutive or separate days (Sun et al. 2021). Data were binned into 7-day periods to examine seasonal dynamics, and iterations were made spanning +/- 91 days at weekly intervals. For diurnal dynamics, hourly data was used directly, and iterations were made spanning +/- 24 hours.

By considering both the optimum identified time lags and the overall strength of the causal relationship, network maps can be constructed to assess how the full suite of variables interact to influence CH_4 fluxes. Conceptually, this is achieved by summarizing the strength of coupling and optimal lag times between all tested variable pairs, including all ancillary variables with only positively identified (significant) connections mapped. In general, direct connectivity is exhibited when the predictive skill is high and lag times are short and indirect connectivity is exhibited when the prediction skill is lower and lag times are long (Fan et al. 2020). We selected ranking categories of high, moderate, and low based on rho values of 0.60-1.0, 0.30-0.59, and 0-0.29, respectively. This technique allows variables with indirect links that may appear to influence CH_4 fluxes to be sorted from variables with highly confident direct causal links, yet it remains difficult to distinguish consistent directionality (i.e., sign positive or negative) of the connection as relationships can vary in time (i.e., state dependence) (Deyle et al., 2016).

285 **2.6 Multivariate Predictive Modeling**

286 As an additional feature and promising application of EDM, we also made model predictions
287 using a newly constructed multivariate EDM model. We used an out-of-sample validation method with
288 2017-2019 as the training interval and 2020-2021 as the prediction interval. Only data from the training
289 period was used to make predictions. Predictor data was scaled to reduce dimensional distortion in the
290 state space. The provided prediction variance based on nearest neighbors in the state space was used to
291 calculate a standard deviation as a metric of uncertainty. We included all variables identified as coupled
292 to CH_4 fluxes by daily CCM analysis: temperature components of soil, water, and air, DO, GPP, H_2O
293 flux, Level, LE, WSpd, PAR, Patm, RH, and Precip. While issues of cross-correlation would potentially
294 violate assumptions for linear models, each of these variables causally impacts CH_4 fluxes in different
295 ways as determined by information embedded in the CH_4 time series. Thus, the inclusion of variables that
296 exhibit cross-correlation is possible with EDM.

297 **3. Results**

298 **3.1 Site Characteristics, Phenology, and CH_4 Fluxes**

299 During the study period (2017-2021), the annual average air temperature (Tair), salinity (Sal), and
300 water level (Level) were 13.9 ± 9.1 ˚C, 8.9 ± 4.1 ppt and 0.25 ± 0.2 m above sea level, respectively with a
301 tidal range of 1.2 m and maximum daily salinity as high as 19.5 ppt. The average annual precipitation
302 (Precip) ranged from 567-779 mm, which is received evenly across the year (Fig. 1) (Tables S1-S3). The
303 growing phenoperiod typically begins with green-up events occurring in April or early May, and
304 dormancy commences with complete vegetation senescence in November. For the reference year utilizing
305 hourly data (2020-21), the dormancy phenoperiod began on October 25th. It ended at the start of the 2021
306 growing phenoperiod on April 26th, which continued until the subsequent dormancy phenoperiod on
307 October 23rd. Despite high levels of GPP, which ranged from 1,412-1,609 g C m^{-2} yr^{-1}, the site was a net

carbon source for four out of the five years (NEE range: -126 to 221 g C m^{-2} yr^{-1}) and was a constant annual source of CH_4 with emissions ranging from 15.4-16.5 g C m^{-2} yr^{-1} (Fig. 1).

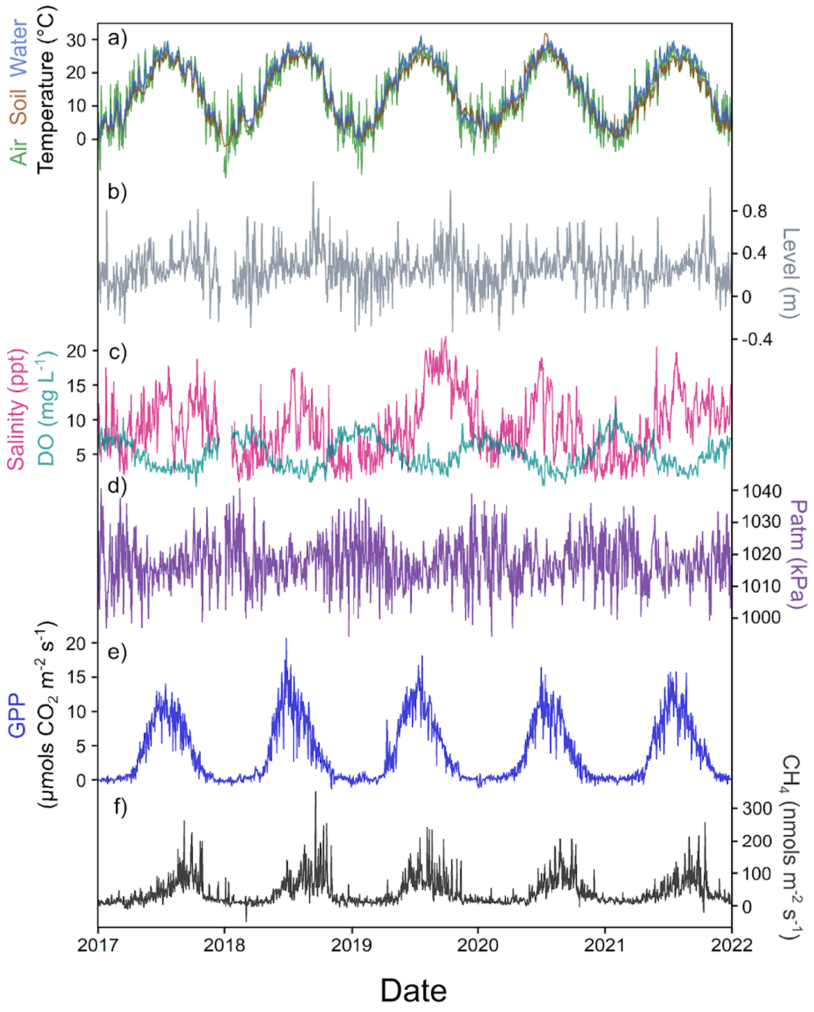

Fig. 1: Time series of mean daily data for top identified predictive drivers and CH_4 flux from 2017-21. a) Air, soil, and water temperature (green, brown, and blue, respectively), b) level (gray), c and d) salinity (pink) and dissolved oxygen (DO) (teal), d) atmospheric pressure (Patm) (purple), e) gross primary productivity (GPP) (blue), and f) CH_4 flux (black).

3.2 CH_4 Time Series Characteristics

We determined that CH_4 is a highly dimensional independent variable that required at least ten dimensions to recreate the original dynamics (Fig. S5). Despite a slightly lower peak at four dimensions, we selected the dimensionality with the greatest predictive skill to capture a full range of potential variable dynamics; because CCM is expected to identify coupling and quantify the overall strength of all possible relationships. Consequently, we confirmed that the response of CH_4 flux was highly dependent on state space or transient ecosystem conditions (i.e., dynamical and nonlinear) (Fig. S6).

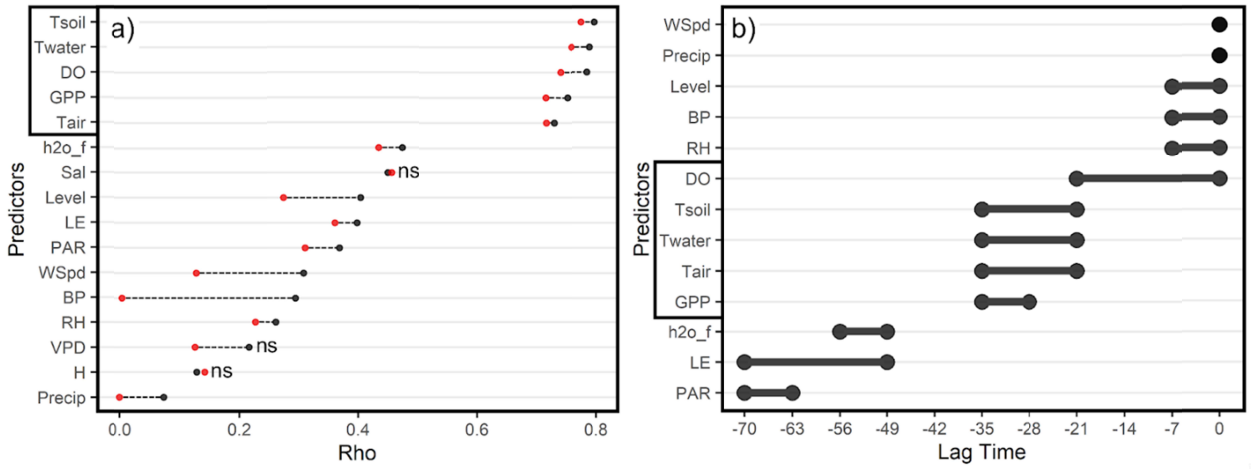

Fig. 2: Results from Convergent cross mapping (CCM) and extended CCM for seasonal dynamics from daily data spanning 2017-21. a) Identification of strongest predictor variables for CH_4 flux using CCM. Red points represent the maximum predictive skill achieved with simulated surrogate data. Black points indicate prediction skill of real data. ns denotes non-significant cross-mapping due to a lack of convergence or overlap with surrogate data results. Outlined variables exhibit a prediction skill > 0.6. b) Optimal time lags (in number of days) determined from extended CCM.

3.3 Causality Analysis with CCM

Examination of daily data with CCM revealed that the top causal variables at the seasonal/multiday scale (rho>0.70) consisted of temperature components (Tsoil, Twater, Tair), DO, and

GPP (Fig. 2a). These select variables were a distinct grouping, with all other variables falling below a threshold of rho=0.50. The remaining variables (H_2O flux, Level, LE, PAR, WSpd, Patm, RH, Precip; sorted from higher to lower coupling strength) were identified as causal (rho=0.10-0.50) except for Sal, VPD, and H, which did not meet convergence criteria or overlapped with surrogate data (Fig. S7). The growing phenoperiod was complex regarding the number of predictors and lags, yet physical factors also played an important role. Examination of hourly data for the diel scale analysis from the growing phenoperiod revealed Level as the top causal variable (rho~0.70), followed by a grouping that included Patm, Sal, DO, and Tsoil (rho=0.30-0.50) (Fig. 3a). The remaining variables (PAR, Twater, RH, GPP, H, H_2O flux, WSpd, LE, VPD, Tair; sorted from higher to lower coupling strength) also had a degree of coupling (rho=0.15-0.25), except Precip (Fig. S8). Examination of hourly data from the dormancy phenoperiod revealed Level, DO, and Sal as top causal variables (rho=0.55-0.30) (Fig. 3c). Most remaining variables (Patm, RH, WSpd, Tair, VPD, PAR, Precip; sorted from higher to lower coupling strength) also exhibited some coupling (rho=0.10-0.20), yet this period contained the largest number of non-significant variables, which included GPP, Tsoil, Twater, H, LE, and water fluxes (Fig. S9).

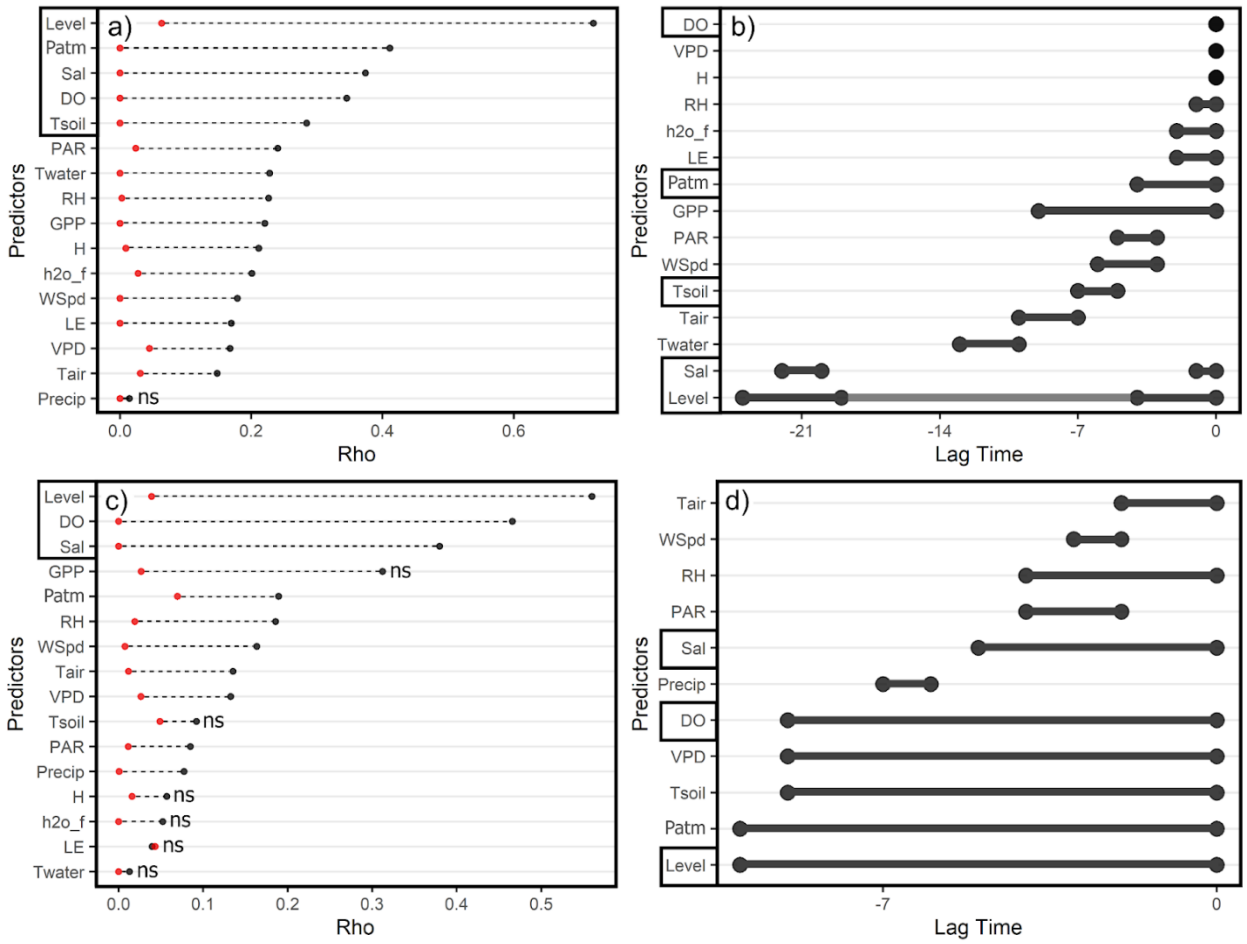

348

349 **Fig. 3:** Results from Convergent cross mapping (CCM) and extended CCM for diurnal/seasonal dynamics
350 from select hourly data spanning 2020-21. a) Growing phenoperiod CCM at maximum library size
351 between all variables and CH_4 flux, b) Growing phenoperiod optimal time lags for extended CCM
352 represented by the number of days (x-axis), c) Dormancy phenoperiod CCM at maximum library size
353 between all variables and CH_4 flux. d) Dormancy phenoperiod optimal time lags for extended CCM
354 represented by the number of days (x-axis). Red points represent the maximum predictive skill achieved
355 with simulated surrogate data. Black points indicate prediction skill of real data. ns denotes non-
356 significant cross-mapping due to a lack of convergence or overlap with surrogate results. Outlined
357 variables exhibit a prediction skill > 0.3.

358

3.4 Optimal Lags with Extended CCM

Implementation of extended CCM revealed that the influence of some variables is more immediate while others are associated with a lag. While any identified lags indicate the optimal time period of causal influence, these lags are not necessarily related to the overall strength of the causal relationship. However, longer lags can mean more indirect relationships within the context of causal network mapping. When applying daily data to unravel seasonal/multiday dynamics, we found that PAR, LE, and H_2O fluxes are associated with the most extended lag times occurring between 49-70 days (seasonal/multiday scale) (moderate causal strength). These were followed by a grouping of top predictor variables identified by the previous CCM analysis (Tsoil, Twater, Tair, GPP) (high causal strength), which were most influential between 21-35 days (monthly scale). The remaining variables (DO, Level, WSpd, Patm, RH, Precip) exerted a close temporal relationship (0 days) at a range of causal strengths, but DO was important over a more extended period (0-3 weeks), followed by Level, Patm, and RH (0-1 week) and finally WSpd and Precip (0 days). However, Precip had the weakest coupling (Fig. 2b) (Fig. S10).

When applying hourly data from the growing phenoperiod to unravel diurnal dynamics, we found that lags were more complex. Both Level and Sal (strong and moderate causal strength, respectively) had peaks occurring between 0-5 hours and again between 19-23 hours, but the influence of Level was also persistent throughout the day (denoted as a gray bar in Fig. 3b). Temperature components had successively shorter lags moving from Twater (9-13 hours) to Tsoil (5-7 hours) and finally Tair (3-6 hours) (all moderate causal strength). The remaining variables were influential immediately (0 hours), with GPP extending the longest (0-9 hours), followed by Patm (0-5 hours), LE and water fluxes (0-3 hours), RH (0-1 hour) and finally DO, VPD, and H (0 hours) (moderate causal strength) (Fig. 3b) (Fig. S11). Lag times were much shorter for the dormancy phenoperiod. Almost all causal variables (Level, DO, Sal, Patm, RH, Tair, VPD, Tsoil) exerted a close temporal relationship (0 hours) with DO, VPD, Tsoil, Patm, and Level active over the most extended period (0-10 hours). Precip was influential between

7-8 hours, yet again had the lowest causal strength while PAR, RH, WSpd, and Tair all exerted influence between 0-5 hours) (moderate causal strength) (Fig. 3d) (Fig. S12).

3.5 Causal Network Mapping

Causal network maps reveal high interconnection among variables at multiple scales (seasonal, multiday, and diurnal) and indicate that fluxes result from a suite of factors. When using daily data, we discovered several interesting patterns (Fig. 4). First, PAR is important for CH_4 (rho=0.66), but its action is likely indirect via greater influence on other relevant variables (e.g., H_2O fluxes and temperature components) (rho=0.65 and 0.90). The strong relationship between GPP and CH_4 fluxes (rho=0.86) was influenced by VPD, Tair, Sal, and DO (rho=0.52-0.82), which are in turn influenced by RH, PAR, and Level, respectively (rho=0.41-0.71). Other variables, such as RH and WSpd, were not causally connected to any variables examined.

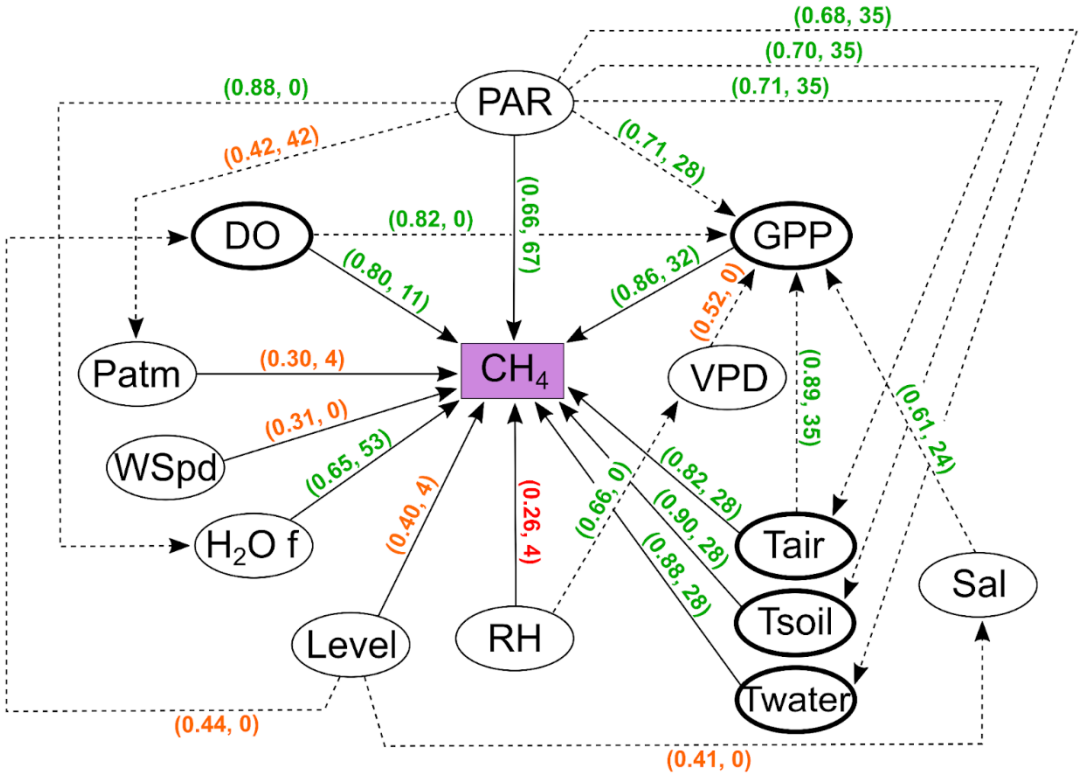

395

396 **Fig. 4:** Causal network map showing seasonal dynamics between all relevant variables for daily data
397 spanning 2017-21. Numbers represent predictive skill followed by the median value of the optimum time
398 lag. Colors represent the strength of coupling, green=strong (0.6-1.0), orange=moderate (0.30-0.59), and
399 red (weak) (0-0.29). Solid lines represent direct relationships, and dashed lines represent indirect
400 relationships. Variables outlined in bold represent the top causal variables identified by CCM analysis.

401 When applying hourly data for the growing phenoperiod, many highly connected variables
402 identified from the seasonal analysis (Temperature components, GPP, DO) exert far less influence (Fig.
403 5a). The water level was the most directly important variable (rho=0.72) and was highly connected to
404 both Sal and DO (rho-0.90-92), which exerted moderate influence on CH_4 fluxes (rho=0.35-0.38). Over
405 seven additional variables provided moderate-low influence, but all showed a similar predictive skill
406 (rho=0.17-0.41), highlighting the complexity associated with the sub-daily growing phenoperiod. Hourly
407 data from the dormancy phenoperiod exhibited the most straightforward network connectivity with the

408 least interdependencies (Fig. 5b). As with growing phenoperiod data, Level was the most directly
409 important variable (rho=0.60) and exerted a strong influence on Sal and DO (rho=0.81-89), which exerted
410 moderate influence on CH_4 fluxes (rho=0.38-0.49). Additional variables were associated with weaker
411 casual relationships (rho=0.12-0.22), and only temperature components, VPD, Patm, Sal, and DO were
412 dependent on the activity of other variables during this phenoperiod.

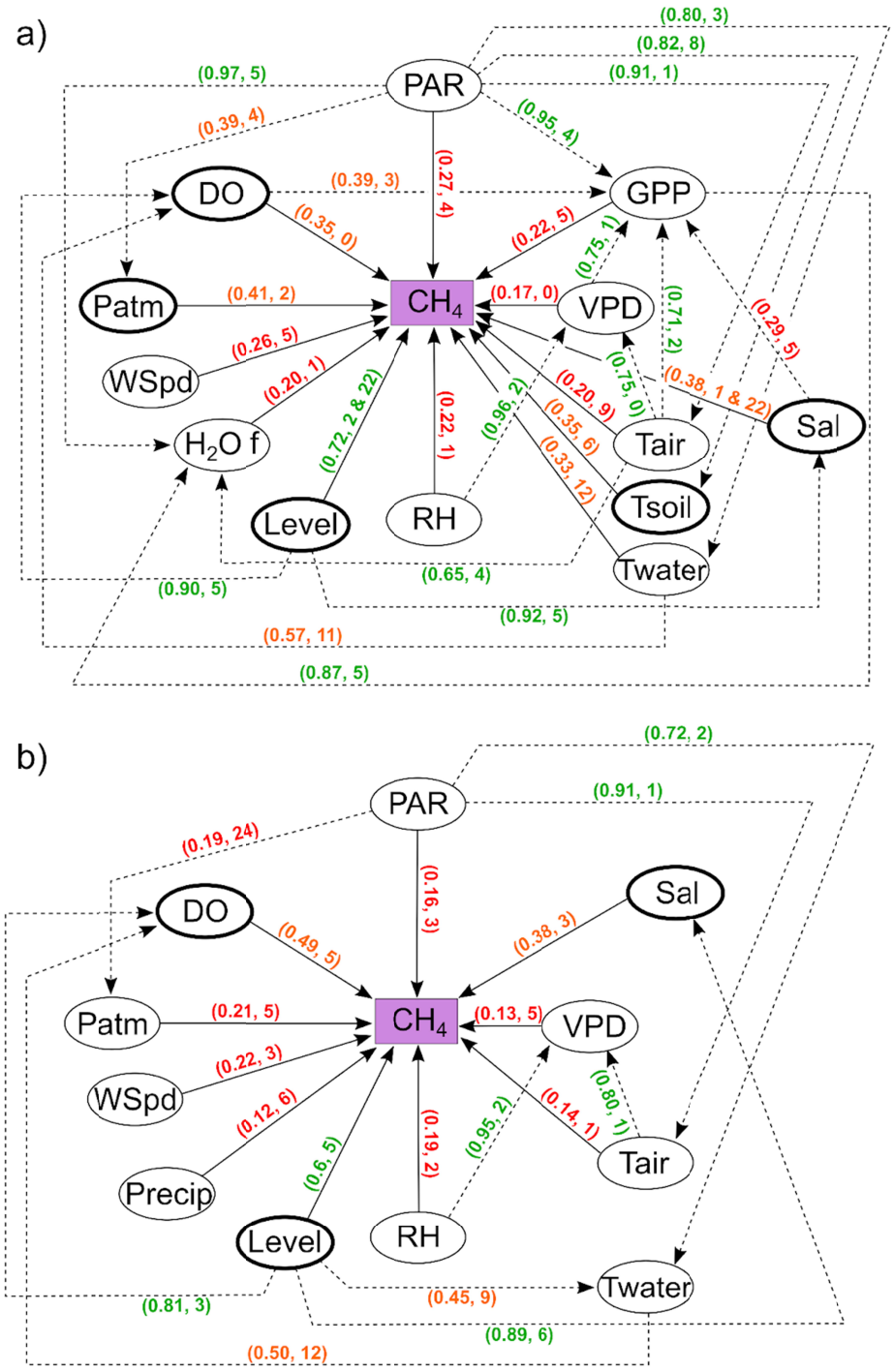

Fig. 5: Causal network maps showing diurnal/seasonal dynamics between all relevant variables for select hourly data spanning 2020-21 for a) Growing phenoperiod and b) Dormancy phenoperiod. Numbers represent predictive skill followed by the median value of the optimum time lag. Colors represent the strength of coupling, green=strong (0.6-1.0), orange=moderate (0.30-0.59), and red (weak) (0-0.29). Solid

lines represent direct relationships, and dashed lines represent indirect relationships. Variables outlined in bold represent the top causal variables identified by CCM analysis.

3.6 Modeling Output

The predictive multivariate EDM model fell within 1% of the expected 2-year annual sum derived from the gap-filled EC benchmark for CH_4 flux (31.6 g C m^{-2}) (Fig. 7). This model incorporated all of the positively coupled variables identified by CCM analysis including temperature components of soil, water, air, GPP, DO, H_2O flux, Level, LE, PAR, WSpd, Patm, RH, and Precip. This generated a 2-year sum of 31.8 g C m^{-2} (0.63% difference; slope 0.57) with an annual uncertainty of +/- 29.3 g C m^{-2}, calculated from the state space. This approach had challenges representing high fluxes during senescence and despite good overall predictions, carried a high overall uncertainty and small over-prediction bias for lower magnitude fluxes (< 50 nmol m^{-2} s^{-1}) (Fig. 6b). It should be noted that the uncertainty estimated for the EDM model is based on the nearest neighbor distance weights within the projected state space and although we scaled predictor variables, including more variables can distort the state space to a greater extent.

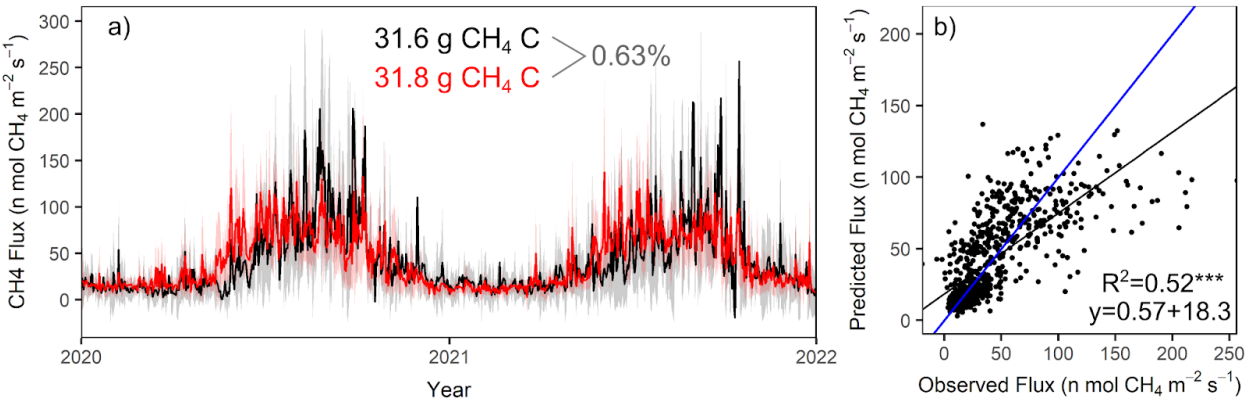

Fig. 6: a) Multivariate EDM modeling results at the daily time step for prediction years 2020-21 and b) linear regression comparisons. Black lines represent daily CH_4 flux measured by eddy covariance (EC) as a benchmark +/- daily sd (grey shading), and red lines represent daily modeled CH_4 flux +/- prediction variance sd (pink shading). The reported black sum is the 2-year total carbon budget from CH_4 calculated

with EC data (benchmark), and the red sum is the 2-year total carbon budget from CH_4 estimated with modeled data and percent difference (gray). The blue line on regression plots is a 1:1 line.

4. Discussion

4.1 Comparisons with Previous Wetland CH_4 Studies

There are limited CH_4 studies in salt marshes but it has been reported by linear methods that temperature, PAR, plant productivity, or some proxy (e.g., GPP, biomass, chlorophyll concentration), water level, and salinity are important predictors for CH_4 fluxes (Abdul-Aziz et al. 2018, Huertas et al. 2019, Martin and Moseman-Valtierra 2017, Poffenbarger et al. 2011.) Despite differing temporal averaging periods (daytime, nighttime, year-round, multi-year) and different model structures (linear regression, multivariate canonical correlation, multivariate generalized least squares), multiple approaches have also been able to identify the importance of temperature, DO, and Patm for CH_4 dynamics (Vázquez-Lule and Vargas 2021, Hill and Vargas 2022). Other multi-site studies have also identified similar predictor variables with both linear and other nonlinear methods, especially temperature components, in non-tidal freshwater wetlands (Knox et al, 2020). The mechanisms supported by additional variables such as water level and GPP are more complex, with influence often manifesting across several temporal scales (Sturtevant et al. 2016). Our results indicate that the effects of GPP are highly dependent on the time domain at multiple scales (seasonal and diurnal) and multivariate interactions among variables. While linear models may be capable of extracting similar variables in many cases, these methods fail to identify dependencies, lags, and complex interrelationships. Thus, linear approaches may still limit our interpretations because the influence of one variable can be the result of indirect influence from a third variable, a phenomenon that can be indirectly inferred when applying CCM.

Several studies based on non-tidal freshwater wetlands have successfully applied alternative nonlinear analysis methods (Knox et al. 2021, Sturtevant et al. 2016) or machine learning approaches such as ANN's or random forest techniques (Rey-Sanchez et al. 2018, Zhu et al. 2013, Abbasi et al. 2019, Zaki and Abdul-Aziz 2022, Morin et al. 2017). In these non-tidal freshwater wetlands, interactions regulating fluxes do not include the same dynamics found within tidal wetlands including frequent oscillation of water level and subsequent modulation of sediment salinity, dissolved oxygen, and redox conditions (Vazquez-Lule and Vargas 2021). Further, dominant vegetation species differ, which can influence the biogeochemical conditions of the sediments and CH_4 production (Seyfferth et al. 2020, Yuan et al. 2016, Gao et al. 2018). Despite differences, these studies also show that the strongest relevant drivers are identified by both linear and nonlinear approaches, yet incomplete results from solely applying linear methods limit the full mechanistic understanding of the system (Sturtevant et al. 2016). Specifically, issues of cross-correlation can restrict which variables are included to satisfy model requirements, and important lags and interrelationships fail to be identified. In fact, tidal saltwater wetlands have been purposely excluded from several FLUXNET- CH_4 analyses because they do not follow the general pattern of linear relationships defined by freshwater wetlands, and an overall lack of data from these highly dynamic ecosystems creates difficulties when attempting to generalize across multiple sites (Chang et al. 2021, Delwiche et al. 2021, Knox et al. 2021).

In limited cases where nonlinear methods are applied, findings largely support our results, demonstrating lags with GPP, temperature, and water level, but with temporal synchrony with VPD and energy fluxes (Delwiche et al. 2021). For example, in a multi-site synthesis study of freshwater sites, median seasonal lags associated with water level extended 17±11 days, 8±16, and 5±14 days for Tair and Tsoil, respectively, and were synchronous for Patm while at the diel scale, GPP was lagged up to 4 hours and energy fluxes and VPD were synchronous (<1 hour) (Knox et al. 2021). A similar study from a forested/shrub wetland found CH_4 lags associated with GPP extending up to 60 days (Turner et al. 2021), potentially indicating different time dependencies based on vegetation type and structure. There is overwhelming evidence supporting that temporal lags exist between multiple environmental variables and

485 CH_4 fluxes across different types of wetlands. Thus, it is important to include methods such as CCM to
486 identify such lags in the context of causality to properly represent the complexity of how biophysical
487 drivers control CH_4 fluxes

488 **4.2 Seasonal CH_4 Dynamics**

489 Seasonal CH_4 dynamics are strongly controlled by temperature components, GPP, and DO,
490 indicating reliance on biological factors. Previous studies showed that predictors such as Level, Patm, and
491 VPD are important in a linear multivariate context but rank lower in causality in the current study
492 (Vázquez-Lule and Vargas 2021, Hill and Vargas 2022). This is likely because these variables are less
493 strongly coupled with CH_4 activity at this scale due to: a) limited occurrence as with transient low-
494 pressure systems, which operate synchronously with CH_4 emissions and rarely exert influence on scales
495 extending beyond several days (Fig. 2b) (Mønster, Kjeldsen, and Scheutz 2019, Tokida et al. 2007, Knox
496 et al. 2021); or b) indirect mechanisms as with Patm and pressurized gas flow (Björn et al. 2022, Zhang
497 and Ding 2011), and VPD limiting stomatal conductance and the possible decrease in plant-mediated
498 transport. At the seasonal scale, temperature is a strong predictor in temperate ecosystems because it
499 regulates the window of active plant growth and belowground microbial metabolic rates (Zhu et al. 2019,
500 Yvon-Durocher et al. 2014), influencing below-ground storage pools and, ultimately, sediment-
501 atmosphere fluxes (Reid et al. 2013, Capooci and Vargas 2022). GPP also has strong coupling and may
502 suggest there is connectivity or flow between plant photoassimilates and methanogens in the rhizosphere,
503 which increases with seasonal biomass development. We observed a 32-day median lag time between
504 GPP and effects on CH_4 flux, similar to the lag identified for temperature (35 days), which may indicate
505 structural changes in the vegetation are responsible for the observed seasonal increase in CH_4 flux.
506 Weaker couplings were associated with physical variables such as Patm and lag times for these variables
507 were much shorter. Thus, it appeared that biological vs. physical processes operate at different temporal
508 scales.

509 Salinity has previously been identified as an important daily-scale predictor by linear modeling
510 but had no direct causal influence on seasonal CH_4 fluxes in this study. While salinity causes direct
511 inhibitory effects for methanogens by limiting the availability of sulfate substrates via microbial
512 competition in most wetlands (Reddy and DeLaune 2008), there is evidence for the presence of
513 methylotrophic bacteria in salt marshes which produce CH_4 from non-competitive substrates resulting in
514 elevated emissions despite the presence of sulfate (Seyfferth et al. 2020, Capooci and Vargas 2022).
515 Evidence to support this phenomenon exists from a variety of wetland studies that either lack *S.*
516 *alterniflora* and thus more closely follow the paradigm of CH_4 inhibition (Chmura, Kellman, and
517 Guntenspergen 2011, Krauss et al. 2016, Poffenbarger et al. 2011), or contain *S. alterniflora* and emit
518 methane above or at the high-end of a widely accepted CH_4-sulfate threshold (Poffenbarger et al2011,
519 Oremland et al. 1982, Huertas et al. 2019, Rosentreter et al. 2021). We propose that the elevated
520 emissions, especially during senescence, are tied to the release of secondary plant compounds (osmolytes)
521 associated with *S. alterniflora,* including glycine betaine and dimethyl sulfoniopropionate which are
522 broken down via fermentation to trimethylamine and dimethyl sulfide and are exclusively utilized by
523 methylotrophic methanogens (Husband and Kiene 2007, Jones et al. 2019). It is also important to note
524 that this marsh rarely experiences salinity extremes over 20ppt, thus sites influenced by higher salinity
525 may experience different characteristics.

526 **4.3 Diurnal CH_4 Dynamics**

527 Diurnal CH_4 dynamics during the growing phenoperiod are controlled by multiple factors with
528 many interdependencies among variables, yet the most important causal variables are Level, Patm, Sal,
529 DO, and Tsoil. This indicates that CH_4 fluxes over the diurnal course are controlled by both biochemical
530 factors likely tied to plant and microbial activity (Sal, DO, Tsoil) and physical factors likely tied to
531 emissions (Level, Patm) (Moore and Roulet 1993, Reid, et al 2015, Knox et al. 2021, Liu et al. 2019).
532 While several studies have made attempts at reducing this level of complexity by applying parsimonious
533 models that only incorporate the most important drivers (via linear methods) (Levy et al. 2012, Abdul-

534 Aziz et al. 2018, Baird et al. 2019), this may only be useful for generating coarse-scale information. Other
535 studies have applied more complex process-based models, although these require an extensive
536 mechanistic understanding and often experience difficulties when moving across study sites (Zhang et al.
537 2020, Li et al. 2016), where interacting variables and driving processes can differ considerably (Krauss et
538 al. 2016, Rosentreter et al. 2021). This can limit the range of potential applications and may be less
539 relevant for coastal wetlands where relationships can differ greatly from site to site.
540 The dormancy phenoperiod is comparatively simple, with the most important causal variables
541 consisting of Level, DO, and Sal. This is also supported by considerably less interconnection between
542 variables. Considering the lack of active vegetation, we can assume mechanisms related to these
543 predictors change in relation to the growing or year-round daily averaging periods (Bansal et al. 2020,
544 Reid et al. 2013). Although the relationship is weak, coupling between CH_4 and Sal increases following
545 the end of senescence and the preceding seasonal peak in emissions. Because vegetation is no longer
546 present, the flow of photoassimilates stops, and availability of osmolyte byproducts likely decreases
547 within sediments. Thus, Sal may become more relevant during dormancy as competition between sulfate-
548 reducing bacteria and methanogens likely increases (Derby et al. 2021, Poffenbarger et al. 2011), while
549 the spatial separation between production zones at depth may be less exposed to sulfate fluctuations from
550 tidal exchange (Koebsch et al. 2019). Further, plant-mediated transport is curtailed, leading to greater
551 importance of conditions at the sediment interface (Wang and Han 2005). This is supported by the lack of
552 causal influence from associated variables such as GPP, LE, and H_2O flux. This also likely explains the
553 importance of DO in tidal waters, which reaches a concentration peak during dormancy, likely
554 influencing CH_4 oxidation rates. In either case, the top hourly predictor for both growing and dormancy
555 phenoperiods is Level that oscillates between low and high tides at six-hour intervals but also shifts on a
556 14-day spring/neap tide and is highly tied to fluctuations of DO and Sal (Vázquez-Lule and Vargas 2021).
557 Our results show that while all these variables are related and often highly cross-correlated with linear
558 methods, each of these variables exerts a unique influence on CH_4 dynamics, yet there is also strong

559 interdependence with how these variables change in time, highlighting the importance of incorporating
560 true nonlinear analysis methods.

561 **4.4 Relevance of Time Lags**

562 On a seasonal/multiday scale, almost all causally significant variables were associated with lag
563 times where influence is exerted across several consecutive days or weeks. The most important causal
564 variables (temperature components and GPP) had medium lag times (i.e., "slow") near 3-5 weeks, likely
565 associated with the possible threshold effect with the temperature-driven initiation of plant growth
566 (O'Connell, Alber and Pennings 2020), or increased production and transport of photoassimilates to the
567 rhizosphere (Knox et al. 2021). This lag time (3 weeks) was also associated with the effect of salinity on
568 GPP, likely indicating increases in plant osmolyte production coinciding with initial spring biomass
569 accumulation (Husband and Kiene 2007, Mulholland and Otte 2000). It is important to recognize that we
570 are measuring CH_4 fluxes (the physical process of release); thus, these observed lags are also likely
571 associated with the disconnection between production and observed fluxes. The shortest lags exert
572 immediate (<1 week) (i.e., "fast") but also prolonged impact extending up to 1 week for Level, Patm, and
573 RH and up to 4 weeks for DO. This effect from Level is likely a result of high/low water levels tied to
574 spring/neap tide cycles, which oscillate on a 6-7 day period. Yet, there are also fluctuations at shorter time
575 periods, both of which impact soil water content and biogeochemical conditions of the sediments
576 (Seyfferth et al. 2020). Tidal waters also directly influence salinity and DO levels within sediments, but
577 the effect of DO is prolonged and likely tied to its strong influence on GPP, as shown by our results (Fig.
578 4). The effects of Patm and RH are likely tied to mesoscale circulation and air mass transit which modify
579 the air column and provide a physical forcing mechanism (Tokida et al. 2007). The longest lag times were
580 associated with LE, H_2O flux, and PAR, which likely represents a major seasonal oscillation driven by
581 solar angle and changes in available radiation (Guo et al. 2010). While only weakly causal, there were no
582 lags associated with WSpd or Precip, indicating an effect exclusively at the sub-daily level as, in most
583 cases, the occurrence of wind or rain rarely extends into multi-day events.

584 During the growing phenoperiod, top causal variables identified by CCM analysis (Level, Patm,
585 Sal, DO, Tsoil) all operated at different peak lag times, highlighting the complexity of observing and
586 measuring fluxes during this time. The most important causal variable (Level) exerts influence over the
587 entire 24-hour period yet peaks in causal effect at 0-5 hours and 20-24 hours, near when Sal (moderately
588 casual) was influential, which is likely tied to semi-diurnal tidal cycling and water levels which are
589 typically higher during nighttime high tide (Forbrich and Giblin 2015). Influence over the entire 24-hour
590 period may be due to a smearing-out effect as the tide shifts its range an hour each day. Patm and DO
591 (moderately causal) were associated with a zero-lag time but the effect of Patm extended up to 5 hours.
592 These lags are likely related to fast (immediate) oxidation activity across sediment, daily pressure
593 fluctuations, and convective flow-through transport of CH_4 via plant-mediated transport driven by solar
594 activity (Kim, Verma and Billesbach 1999, Ding and Cai 2007). Although the overall causality was
595 weaker and distributed across variables, many of the fast variables during the growing phenoperiod are
596 related to energy exchange dynamics (LE and H) and tied to changes in evapotranspiration (H_2O flux,
597 VPD, RH). This is likely explained by combined evaporation from saturated sediments where CH_4 has
598 accumulated in porewater, evaporation from areas of open water that receive a lateral influx of dissolved
599 CH_4, and plant-mediated transport factors reliant on stomatal activity, which channel dissolved CH_4 in the
600 transpiration stream (Megonigal and Guenther 2008, Sun et al. 2012, Trifunovic et al. 2020). GPP is both
601 a fast and slow variable indicating a supply of photoassimilates is triggered upon initiation of morning
602 photosynthesis but with lags extending up to 8 hours when photosynthesis gears down in the evening.
603 During the dormancy phenoperiod, top causal variables identified by CCM analysis (Level, Sal,
604 DO) all had immediate influence but were influential at lag times extending up to 5-10 hours, highlighting
605 the importance of tidal activity and modulation of associated variables (Sal and DO). While the remaining
606 variables were only weakly causal, several interesting patterns exist. In contrast to the slower effect of
607 Tair during the growing phenoperiod, Tair was a fast variable with short lag times in dormancy, while the
608 effect of Tsoil had longer lags, up to 9 hours, indicating a connection to microbial activity and
609 temperature thresholds associated with CH_4 production (Chadburn et al. 2020). All top causal variables

were related to tidal activity (Level, DO, Sal), indicating that hydrological factors and the riverine-ocean connectivity become crucial during the dormancy phenoperiod. The shorter lag times during this phenoperiod may also indicate more direct coupling with physical factors and less complex interactions involving the presence of vegetation, such as substrate supply and plant-mediated transport (Vázquez-Lule and Vargas 2021). Taken together, these results highlight the multi-mechanistic activities and processes which regulate CH_4 fluxes.

4.5 Multivariate EDM Modeling

This study demonstrates high complexity in the biophysical controls of CH_4 fluxes in tidal wetlands. These results are based on high-frequency measurements and long-term observations (5 years) that contribute to our understanding of CH_4 dynamics. The multivariate EDM mode provided predictions within 1% of the CH_4 carbon sum measured from the EC benchmark. This model captured most of the higher magnitude fluctuations and high emission peaks during the growing phenoperiod, yet omitted higher magnitude fluctuations during senescence. Despite good performance, this model still considerably underpredicted during senescence and overpredicted during green-up. Consequently, these transitions represent a challenge as rapid metabolic and structural changes happen in the plant canopy (Vazquez-Lule et al 2022). Although we included the full suite of identified causal variables from CCM, this could indicate that additional variables omitted or not measured (e.g., sediment redox potential, biomass, sediment substrate availability) are essential to explain these unusually high fluxes during senescence.

5. Conclusion

We demonstrate that nonlinear state space methods uncover the complex dynamics and interdependencies among predictors and their influence on CH_4 flux. The technique can tease apart not only the strength of causal variables but also identify lags, and complex interconnections among the full suite of measured variables as past information about driving variables becomes embedded within the presently observed CH_4 time series. Overall, CCM was able to identify and rank multiple causal variables while providing a holistic picture of variable interactions and lagged relationships, which is critical for an

635 accurate mechanistic understanding of system behavior. We highlight that CCM is a powerful technique
636 that provides mechanistic information regarding causality, lags, and interconnectivity among an extensive
637 collection of potentially important variables. Therefore, by complementing CCM with multivariate EDM
638 we can generate interpretable empirical models that provide insights into controlling mechanisms of
639 ecosystem processes.
640

641 **Acknowledgments**

642 This research was supported by the National Science Foundation (#1652594) and the US
643 Department of Energy (#DE-SC0023099 and #DE-SC0022185). We thank the onsite support
644 from the Delaware National Estuarine Research Reserve (DNERR). The authors acknowledge
645 the land on which they conducted this study is the traditional home of the Lenni-Lenape tribal
646 nation (Delaware nation).
647

648 **Open Research**

649 Meteorological (station: delsjmet-p) and water quality (station: Aspen Landing) data are
650 available from the National Estuarine Research Reserve's Centralized Data Management Office
651 (CDMO) at https://cdmo.baruch.sc.edu/. Phenological data are available from the PhenoCam
652 network (site: stjones) at https://phenocam.sr.unh.edu/webcam/sites/stjones/. Eddy covariance
653 data are available via AmeriFlux (US-StJ; https://ameriflux.lbl.gov/sites/siteinfo/US-StJ).
654

References

Abbasi, T., T. Abbasi, C. Luithui & S. A. Abbasi (2019) Modelling Methane and Nitrous Oxide Emissions from Rice Paddy Wetlands in India Using Artificial Neural Networks (ANNs). *Water,* 11.

Abdul-Aziz, O. I., K. S. Ishtiaq, J. W. Tang, S. Moseman-Valtierra, K. D. Kroeger, M. E. Gonneea, J. Mora & K. Morkeski (2018) Environmental Controls, Emergent Scaling, and Predictions of Greenhouse Gas (GHG) Fluxes in Coastal Salt Marshes. *Journal of Geophysical Research-Biogeosciences,* 123**,** 2234-2256.

Al-Haj, A. N. & R. W. Fulweiler (2020) A synthesis of methane emissions from shallow vegetated coastal ecosystems. *Global Change Biology,* 26**,** 2988-3005.

Baird, A., S. Green, E. Brown & G. Dooling (2019) Modelling time-integrated fluxes of CO2 and CH4 in peatlands: A review. *Mires and Peat,* 24.

Baldocchi, D. D. (2003) Assessing the eddy covariance technique for evaluating carbon dioxide exchange rates of ecosystems: past, present and future. *Global Change Biology,* 9**,** 479-492.

Bansal, S., O. F. Johnson, J. Meier & X. Zhu (2020) Vegetation Affects Timing and Location of Wetland Methane Emissions. *Journal of Geophysical Research: Biogeosciences,* 125**,** e2020JG005777.

Barba, J., A. Cueva, M. Bahn, G. A. Barron-Gaffordd, B. Bond-Lamberty, P. J. Hanson, A. Jaimes, L. Kulmala, J. Pumpanen, R. L. Scott, G. Wohlfahrt & R. Vargas (2018) Comparing ecosystem and soil respiration: Review and key challenges of tower-based and soil measurements. *Agricultural and Forest Meteorology,* 249**,** 434-443.

Barton, K. & M. K. Barton (2015) Package 'mumin'. *Version,* 1**,** 439.

Bridgham, S. D., H. Cadillo-Quiroz, J. K. Keller & Q. L. Zhuang (2013) Methane emissions from wetlands: biogeochemical, microbial, and modeling perspectives from local to global scales. *Global Change Biology,* 19**,** 1325-1346.

Capooci, M. & R. Vargas (2022) Trace gas fluxes from tidal salt marsh soils: implications for carbon-sulfur biogeochemistry. *Biogeosciences,* 19**,** 4655-4670.

Chadburn, S. E., T. Aalto, M. Aurela, D. Baldocchi, C. Biasi, J. Boike, E. J. Burke, E. Comyn-Platt, A. J. Dolman, C. Duran-Rojas, Y. Fan, T. Friborg, Y. Gao, N. Gedney, M. Göckede, G. D. Hayman, D. Holl, G. Hugelius, L. Kutzbach, H. Lee, A. Lohila, F.-J. W. Parmentier, T. Sachs, N. J. Shurpali & S. Westermann (2020) Modeled Microbial Dynamics Explain the Apparent Temperature Sensitivity of Wetland Methane Emissions. *Global Biogeochemical Cycles,* 34**,** e2020GB006678.

Chang, C.-W., M. Ushio & C.-h. Hsieh (2017) Empirical dynamic modeling for beginners. *Ecological Research,* 32**,** 785-796.

Christensen, T. R., A. Ekberg, L. Ström, M. Mastepanov, N. Panikov, M. Öquist, B. H. Svensson, H. Nykänen, P. J. Martikainen & H. Oskarsson (2003) Factors controlling large scale variations in methane emissions from wetlands. *Geophysical Research Letters,* 30.

690 Chu, X. J., G. X. Han, Q. H. Xing, J. Y. Xia, B. Y. Sun, J. B. Yu & D. J. Li (2018) Dual effect of
691 precipitation redistribution on net ecosystem CO2 exchange of a coastal wetland in the Yellow River
692 Delta. *Agricultural and Forest Meteorology,* 249**,** 286-296.

693 Dean, J. F., J. J. Middelburg, T. Röckmann, R. Aerts, L. G. Blauw, M. Egger, M. S. M. Jetten, A. E. E. de
694 Jong, O. H. Meisel, O. Rasigraf, C. P. Slomp, M. H. in't Zandt & A. J. Dolman (2018) Methane
695 Feedbacks to the Global Climate System in a Warmer World. *Reviews of Geophysics,* 56**,** 207-250.

696 Delwiche, K. B., S. H. Knox, A. Malhotra, E. Fluet-Chouinard, G. McNicol, S. Feron, Z. Ouyang, D.
697 Papale, C. Trotta, E. Canfora, Y. W. Cheah, D. Christianson, M. C. R. Alberto, P. Alekseychik, M.
698 Aurela, D. Baldocchi, S. Bansal, D. P. Billesbach, G. Bohrer, R. Bracho, N. Buchmann, D. I. Campbell,
699 G. Celis, J. Chen, W. Chen, H. Chu, H. J. Dalmagro, S. Dengel, A. R. Desai, M. Detto, H. Dolman, E.
700 Eichelmann, E. Euskirchen, D. Famulari, K. Fuchs, M. Goeckede, S. Gogo, M. J. Gondwe, J. P.
701 Goodrich, P. Gottschalk, S. L. Graham, M. Heimann, M. Helbig, C. Helfter, K. S. Hemes, T. Hirano, D.
702 Hollinger, L. Hörtnagl, H. Iwata, A. Jacotot, G. Jurasinski, M. Kang, K. Kasak, J. King, J. Klatt, F.
703 Koebsch, K. W. Krauss, D. Y. F. Lai, A. Lohila, I. Mammarella, L. Belelli Marchesini, G. Manca, J. H.
704 Matthes, T. Maximov, L. Merbold, B. Mitra, T. H. Morin, E. Nemitz, M. B. Nilsson, S. Niu, W. C.
705 Oechel, P. Y. Oikawa, K. Ono, M. Peichl, O. Peltola, M. L. Reba, A. D. Richardson, W. Riley, B. R. K.
706 Runkle, Y. Ryu, T. Sachs, A. Sakabe, C. R. Sanchez, E. A. Schuur, K. V. R. Schäfer, O. Sonnentag, J. P.
707 Sparks, E. Stuart-Haëntjens, C. Sturtevant, R. C. Sullivan, D. J. Szutu, J. E. Thom, M. S. Torn, E. S.
708 Tuittila, J. Turner, M. Ueyama, A. C. Valach, R. Vargas, A. Varlagin, A. Vazquez-Lule, et al. (2021)
709 FLUXNET-CH4: a global, multi-ecosystem dataset and analysis of methane seasonality from freshwater
710 wetlands. *Earth Syst. Sci. Data,* 13**,** 3607-3689.

711 Deyle, E. R., May, R. M., Munch, S. B., & Sugihara, G. (2016). Tracking and forecasting ecosystem
712 interactions in real time. *Proc Biol Sci*, *283*(1822).

713 Derby, R. K., B. A. Needelman, A. A. Roden & J. P. Megonigal (2021) Stratifying by Vegetation and
714 Hydrology Improves Tidal Marsh Methane Emission Accounting.

715 Fan, H., Y. Meng, D. Wang, Y. Zhao & C. Zhao. 2020.. In *2020 35th Youth Academic Annual*
716 *Conference of Chinese Association of Automation (YAC)*, 347-352. IEEE.

717 Filippa, G., E. Cremonese, M. Migliavacca, M. Galvagno, M. Forkel, L. Wingate, E. Tomelleri, U. Morra
718 di Cella & A. D. Richardson (2016) Phenopix: A R package for image-based vegetation phenology.
719 *Agricultural and Forest Meteorology,* 220**,** 141-150.

720 Gao, G. F., P. F. Li, Z. J. Shen, Y. Y. Qin, X. M. Zhang, K. Ghoto, X. Y. Zhu & H. L. Zheng (2018)
721 Exotic Spartina alterniflora invasion increases CH4 while reduces CO2 emissions from mangrove wetland
722 soils in southeastern China. *Scientific Reports,* 8.

723 Geoghegan, E. K., J. S. Caplan, F. N. Leech, P. E. Weber, C. E. Bauer & T. J. Mozdzer (2018) Nitrogen
724 enrichment alters carbon fluxes in a New England salt marsh. *Ecosystem Health and Sustainability,* 4**,**
725 277-287.

726 Glagolev, M. V., O. R. Kotsyurbenko, A. F. Sabrekov, Y. V. Litti & I. E. Terentieva (2021)
727 Methodologies for Measuring Microbial Methane Production and Emission from Soils-A Review.
728 *Microbiology,* 90**,** 1-19.

729 Granger, C. W. (1969) Investigating causal relations by econometric models and cross-spectral methods.
730 *Econometrica: journal of the Econometric Society***,** 424-438.

731 Granse, D., J. Titschack, M. Ainouche, K. Jensen & K. Koop-Jakobsen (2022) Subsurface aeration of
732 tidal wetland soils: Root-system structure and aerenchyma connectivity in Spartina (Poaceae). *Science of*
733 *The Total Environment,* 802**,** 149771.

734 Guo, H. Q., B. Zhao, J. Q. Chen, Y. E. Yan, B. Li & J. K. Chen (2010) Seasonal Changes of Energy
735 Fluxes in an Estuarine Wetland of Shanghai, China. *Chinese Geographical Science,* 20**,** 23-29.

736 Guo, Z., M. Hao, B. Yu & B. Yao (2022) Detecting delay propagation in regional air transport systems
737 using convergent cross mapping and complex network theory. *Transportation Research Part E: Logistics*
738 *and Transportation Review,* 157**,** 102585.

739 Helfter, C., M. Gondwe, M. Murray-Hudson, A. Makati, M. F. Lunt, P. I. Palmer & U. Skiba (2022)
740 Phenology is the dominant control of methane emissions in a tropical non-forested wetland. *Nature*
741 *Communications,* 13**,** 133.

742 Hill, A. & R. Vargas. 2021. Methane and Carbon Dioxide Fluxes in a Temperate Salt Marsh:
743 Comparisons Between Plot, Ecosystem and Component Measurements. B25C-1465.

744 Hill, A. C. & R. Vargas (2022) Methane and Carbon Dioxide Fluxes in a Temperate Tidal Salt Marsh:
745 Comparisons Between Plot and Ecosystem Measurements. *Journal of Geophysical Research:*
746 *Biogeosciences,* 127**,** e2022JG006943.

747 Hsieh, C.-h., S. M. Glaser, A. J. Lucas & G. Sugihara (2005) Distinguishing random environmental
748 fluctuations from ecological catastrophes for the North Pacific Ocean. *Nature,* 435**,** 336-340.

749 Huertas, I. E., M. de la Paz, F. F. Perez, G. Navarro & S. Flecha (2019) Methane Emissions From the Salt
750 Marshes of Donana Wetlands: Spatio-Temporal Variability and Controlling Factors. *Frontiers in Ecology*
751 *and Evolution,* 7.

752 Husband, J. D. & R. P. Kiene (2007) Occurrence of dimethylsulfoxide in leaves, stems, and roots of
753 Spartina alterniflora. *Wetlands,* 27**,** 224-229.

754 Jackson, R. B., M. Saunois, P. Bousquet, J. G. Canadell, B. Poulter, A. R. Stavert, P. Bergamaschi, Y.
755 Niwa, A. Segers & A. Tsuruta (2020) Increasing anthropogenic methane emissions arise equally from
756 agricultural and fossil fuel sources. *Environmental Research Letters,* 15**,** 071002.

757 Jones, H. J., Kröber, E., Stephenson, J., Mausz, M. A., Jameson, E., Millard, A., Purdy, K. J., & Chen, Y.
758 (2019) A new family of uncultivated bacteria involved in methanogenesis from the ubiquitous osmolyte
759 glycine betaine in coastal saltmarsh sediments. *Microbiome*, 7(1), 120.

760 Kim, D. S. (2007) Greenhouse Gas (CH4, CO2, N2O) Emissions from Estuarine Tidal and Wetland and
761 Their Characteristics. *Journal of Korean Society for Atmospheric Environment,* 23**,** 225-241.

762 Kim, Y., M. S. Johnson, S. H. Knox, T. A. Black, H. J. Dalmagro, M. Kang, J. Kim & D. Baldocchi
763 (2020) Gap-filling approaches for eddy covariance methane fluxes: A comparison of three machine
764 learning algorithms and a traditional method with principal component analysis. *Global Change Biology,*
765 26**,** 1499-1518.

766 Knox, S. H., S. Bansal, G. McNicol, K. Schafer, C. Sturtevant, M. Ueyama, A. C. Valach, D. Baldocchi,
767 K. Delwiche & A. R. Desai (2021) Identifying dominant environmental predictors of freshwater wetland
768 methane fluxes across diurnal to seasonal time scales. *Global change biology*.

769 Knox, S. H., J. H. Matthes, C. Sturtevant, P. Y. Oikawa, J. Verfaillie & D. Baldocchi (2016) Biophysical
770 controls on interannual variability in ecosystem-scale CO2 and CH4 exchange in a California rice paddy.
771 *Journal of Geophysical Research-Biogeosciences,* 121**,** 978-1001.

772 Koebsch, F., M. Winkel, S. Liebner, B. Liu, J. Westphal, I. Schmiedinger, A. Spitzy, M. Gehre, G.
773 Jurasinski, S. Köhler, V. Unger, M. Koch, T. Sachs & M. E. Böttcher (2019) Sulfate deprivation triggers
774 high methane production in a disturbed and rewetted coastal peatland. *Biogeosciences,* 16**,** 1937-1953.

775 Krauss, K. W., G. O. Holm, B. C. Perez, D. E. McWhorter, N. Cormier, R. F. Moss, D. J. Johnson, S. C.
776 Neubauer & R. C. Raynie (2016) Component greenhouse gas fluxes and radiative balance from two
777 deltaic marshes in Louisiana: Pairing chamber techniques and eddy covariance. *Journal of Geophysical*
778 *Research-Biogeosciences,* 121**,** 1503-1521.

779 Kuhn, M. (2008) Building Predictive Models in R Using the caret Package. *Journal of Statistical*
780 *Software,* 28**,** 1 - 26.

781 Lakomiec, P., J. Holst, T. Friborg, P. Crill, N. Rakos, N. Kljun, P. O. Olsson, L. Eklundh, A. Persson & J.
782 Rinne (2021) Field-scale CH4 emission at a subarctic mire with heterogeneous permafrost thaw status.
783 *Biogeosciences,* 18**,** 5811-5830.

784 Levy, P. E., A. Burden, M. D. Cooper, K. J. Dinsmore, J. Drewer, C. Evans, D. Fowler, J. Gaiawyn, A.
785 Gray & S. K. Jones (2012) Methane emissions from soils: synthesis and analysis of a large UK data set.
786 *Global Change Biology,* 18**,** 1657-1669.

787 Li, C. (2007) Quantifying greenhouse gas emissions from soils: Scientific basis and modeling approach.
788 *Soil Science and Plant Nutrition,* 53**,** 344-352.

789 Li, T. T., B. H. Xie, G. C. Wang, W. Zhang, Q. Zhang, T. Vesala & M. Raivonen (2016) Field-scale
790 simulation of methane emissions from coastal wetlands in China using an improved version of
791 CH4MOD(wetland). *Science of the Total Environment,* 559**,** 256-267.

792 Li, Y., D. Wang, Z. Chen, J. Chen, H. Hu & R. Wang (2021) Methane Emissions during the Tide Cycle
793 of a Yangtze Estuary Salt Marsh. *Atmosphere,* 12**,** 245.

794 Liu, L. J., D. Q. Wang, S. Chen, Z. J. Yu, Y. K. Xu, Y. Li, Z. M. Ge & Z. L. Chen (2019) Methane
795 Emissions from Estuarine Coastal Wetlands: Implications for Global Change Effect. *Soil Science Society*
796 *of America Journal,* 83**,** 1368-1377.

797 Martin, R. M. & S. Moseman-Valtierra (2017) Different short-term responses of greenhouse gas fluxes
798 from salt marsh mesocosms to simulated global change drivers. *Hydrobiologia,* 802**,** 71-83.

799 McKenna, T., J. Callahan, C. Medlock & N. Bates (2018) Creation of improved accuracy LiDAR-based
800 digital elevation models for the St. Jones River and Blackbird Creek Watersheds. *Newark: Delaware*
801 *Geologic Survey, Technical Report***,** 1-30.

802 Mitra, B., K. Minick, G. Miao, J.-C. Domec, P. Prajapati, S. G. McNulty, G. Sun, J. S. King & A.
803 Noormets (2020) Spectral evidence for substrate availability rather than environmental control of methane
804 emissions from a coastal forested wetland. *Agricultural and Forest Meteorology,* 291**,** 108062.

805 Mønster, J., P. Kjeldsen & C. Scheutz (2019) Methodologies for measuring fugitive methane emissions
806 from landfills – A review. *Waste Management,* 87**,** 835-859.

807 Moore, T. R. & N. T. Roulet (1993) Methane flux: Water table relations in northern wetlands.
808 *Geophysical Research Letters,* 20**,** 587-590.

809 Morin, T. H. (2019) Advances in the Eddy Covariance Approach to CH4 Monitoring Over Two and a
810 Half Decades. *Journal of Geophysical Research-Biogeosciences,* 124**,** 453-460.

811 Morin, T. H., G. Bohrer, L. Naor-Azrieli, S. Mesi, W. T. Kenny, W. J. Mitsch & K. V. R. Schafer (2014)
812 The seasonal and diurnal dynamics of methane flux at a created urban wetland. *Ecological Engineering,*
813 72**,** 74-83.

814 Morin, T. H., G. Bohrer, K. C. Stefanik, A. C. Rey-Sanchez, A. M. Matheny & W. J. Mitsch (2017)
815 Combining eddy-covariance and chamber measurements to determine the methane budget from a small,
816 heterogeneous urban floodplain wetland park. *Agricultural and Forest Meteorology,* 237**,** 160-170.

817 Mulholland, M. M., & Otte, M. L. (2000) Effects of varying sulphate and nitrogen supply on DMSP and
818 glycine betaine levels in Spartina anglica. *Journal of Sea Research*, *43*(3-4), 199-207.

819 O'Connell, J. L., M. Alber & S. C. Pennings (2020) Microspatial Differences in Soil Temperature Cause
820 Phenology Change on Par with Long-Term Climate Warming in Salt Marshes. *Ecosystems,* 23**,** 498-510.

821 Oikawa, P. Y., G. D. Jenerette, S. H. Knox, C. Sturtevant, J. Verfaillie, I. Dronova, C. M. Poindexter, E.
822 Eichelmann & D. D. Baldocchi (2017) Evaluation of a hierarchy of models reveals importance of
823 substrate limitation for predicting carbon dioxide and methane exchange in restored wetlands. *Journal of*
824 *Geophysical Research-Biogeosciences,* 122**,** 145-167.

825 Paparella, F. (2005) Filling gaps in chaotic time series. *Physics Letters A,* 346**,** 47-53.

826 Pinheiro, J., D. Bates, S. DebRoy, D. Sarkar, S. Heisterkamp, B. Van Willigen & R. Maintainer (2017)
827 Package 'nlme'. *Linear and nonlinear mixed effects models, version,* 3.

828 Poffenbarger, H. J., B. A. Needelman & J. P. Megonigal (2011) Salinity Influence on Methane Emissions
829 from Tidal Marshes. *Wetlands,* 31**,** 831-842.

830 Reichstein, M., E. Falge, D. Baldocchi, D. Papale, M. Aubinet, P. Berbigier, C. Bernhofer, N. Buchmann,
831 T. Gilmanov, A. Granier, T. Grünwald, K. Havránková, H. Ilvesniemi, D. Janous, A. Knohl, T. Laurila,
832 A. Lohila, D. Loustau, G. Matteucci, T. Meyers, F. Miglietta, J.-M. Ourcival, J. Pumpanen, S. Rambal, E.
833 Rotenberg, M. Sanz, J. Tenhunen, G. Seufert, F. Vaccari, T. Vesala, D. Yakir & R. Valentini (2005) On
834 the separation of net ecosystem exchange into assimilation and ecosystem respiration: review and
835 improved algorithm. *Global Change Biology,* 11**,** 1424-1439.

836 Reid, M. C., D. S. Pal & P. R. Jaffe (2015) Dissolved gas dynamics in wetland soils: Root-mediated gas
837 transfer kinetics determined via push-pull tracer tests. *Water Resources Research,* 51**,** 7343-7357.

838 Reid, M. C., R. Tripathee, K. V. R. Schafer & P. R. Jaffe (2013) Tidal marsh methane dynamics:
839 Difference in seasonal lags in emissions driven by storage in vegetated versus unvegetated sediments.
840 *Journal of Geophysical Research-Biogeosciences,* 118**,** 1802-1813.

841 Rey-Sanchez, A. C., T. H. Morin, K. C. Stefanik, K. Wrighton & G. Bohrer (2018) Determining total
842 emissions and environmental drivers of methane flux in a Lake Erie estuarine marsh. *Ecological*
843 *Engineering,* 114**,** 7-15.

Rosentreter, J. A., A. N. Al-Haj, R. W. Fulweiler & P. Williamson (2021) Methane and Nitrous Oxide Emissions Complicate Coastal Blue Carbon Assessments. *Global Biogeochemical Cycles,* 35**,** e2020GB006858.

Schiecke, K., B. Pester, M. Feucht, L. Leistritz & H. Witte. 2015. Convergent Cross Mapping: Basic concept, influence of estimation parameters and practical application. In *2015 37th Annual International Conference of the IEEE Engineering in Medicine and Biology Society (EMBC)*, 7418-7421.

Seyfferth, A. L., F. Bothfeld, R. Vargas, J. W. Stuckey, J. Wang, K. Kearns, H. A. Michael, J. Guimond, X. Yu & D. L. Sparks (2020) Spatial and temporal heterogeneity of geochemical controls on carbon cycling in a tidal salt marsh. *Geochimica et Cosmochimica Acta,* 282**,** 1-18.

Stavert, A. R., M. Saunois, J. G. Canadell, B. Poulter, R. B. Jackson, P. Regnier, R. Lauerwald, P. A. Raymond, G. H. Allen, P. K. Patra, P. Bergamaschi, P. Bousquet, N. Chandra, P. Ciais, A. Gustafson, M. Ishizawa, A. Ito, T. Kleinen, S. Maksyutov, J. McNorton, J. R. Melton, J. Müller, Y. Niwa, S. Peng, W. J. Riley, A. Segers, H. Tian, A. Tsuruta, Y. Yin, Z. Zhang, B. Zheng & Q. Zhuang (2022) Regional trends and drivers of the global methane budget. *Global Change Biology,* 28**,** 182-200.

Strom, L., J. M. Falk, K. Skov, M. Jackowicz-Korczynski, M. Mastepanov, T. R. Christensen, M. Lund & N. M. Schmidt (2015) Controls of spatial and temporal variability in CH4 flux in a high arctic fen over three years. *Biogeochemistry,* 125**,** 21-35.

Sugihara, G., R. May, H. Ye, C.-h. Hsieh, E. Deyle, M. Fogarty & S. Munch (2012) Detecting causality in complex ecosystems. *science,* 338**,** 496-500.

Sugihara, G. & R. M. May (1990) Nonlinear forecasting as a way of distinguishing chaos from measurement error in time series. *Nature,* 344**,** 734-741.

Sun, X., W. Fang, X. Gao, S. An, S. Liu & T. Wu (2021) Time-varying causality inference of different nickel markets based on the convergent cross mapping method. *Resources Policy,* 74**,** 102385.

Swain, C. K., P. Bhattacharyya, A. K. Nayak, N. R. Singh, S. Neogi, D. Chatterjee & H. Pathak (2018) Dynamics of net ecosystem methane exchanges on temporal scale in tropical lowland rice. *Atmospheric Environment,* 191**,** 291-301.

Takens, F. 1981. Detecting strange attractors in turbulence. In *Dynamical systems and turbulence, Warwick 1980*, 366-381. Springer.

Tokida, T., T. Miyazaki, M. Mizoguchi, O. Nagata, F. Takakai, A. Kagemoto & R. Hatano (2007) Falling atmospheric pressure as a trigger for methane ebullition from peatland. *Global Biogeochemical Cycles,* 21.

Tong, C., W. Q. Wang, C. S. Zeng & R. Marrs (2010) Methane (CH4) emission from a tidal marsh in the Min River estuary, southeast China. *Journal of Environmental Science and Health Part a-Toxic/Hazardous Substances & Environmental Engineering,* 45**,** 506-516.

Tsonis, A. A., E. R. Deyle, H. Ye & G. Sugihara. 2018. Convergent Cross Mapping: Theory and an Example. In *Advances in Nonlinear Geosciences,* ed. A. A. Tsonis, 587-600. Cham: Springer International Publishing.

Turner, J., A. R. Desai, J. Thom & K. P. Wickland (2021) Lagged Wetland CH4 Flux Response in a Historically Wet Year. *Journal of Geophysical Research: Biogeosciences,* 126**,** e2021JG006458.

Ushio, M. & K. Kawatsu. 2020. Forecasting Ecological Time Series Using Empirical Dynamic Modeling: A Tutorial for Simplex Projection and S-map. In *Diversity of Functional Traits and Interactions: Perspectives on Community Dynamics,* ed. A. Mougi, 193-213. Singapore: Springer Singapore.

Vázquez-Lule, A. & R. Vargas (2021) Biophysical drivers of net ecosystem and methane exchange across phenological phases in a tidal salt marsh. *Agricultural and Forest Meteorology,* 300**,** 108309.

Vázquez-Lule, A., A. L. Seyfferth, M. A. Limmer, P. Mey, M. Guevara, and R. Vargas. 2022. Hyperspectral reflectance for measuring canopy-level nutrients and photosynthesis in a salt marsh. Journal of geophysical research. *Biogeosciences,* 127.

Villa, J. A., Y. Ju, T. Stephen, C. Rey-Sanchez, K. C. Wrighton & G. Bohrer (2020) Plant-mediated methane transport in emergent and floating-leaved species of a temperate freshwater mineral-soil wetland. *Limnology and Oceanography,* 65**,** 1635-1650.

Villa, J. A., Y. Ju, C. Vines, C. Rey-Sanchez, T. H. Morin, K. C. Wrighton & G. Bohrer (2019) Relationships Between Methane and Carbon Dioxide Fluxes in a Temperate Cattail-Dominated Freshwater Wetland. *Journal of Geophysical Research-Biogeosciences,* 124**,** 2076-2089.

Wang, D. Q., Z. L. Chen & S. Y. Xu (2009) Methane emission from Yangtze estuarine wetland, China. *Journal of Geophysical Research-Biogeosciences,* 114.

Wang, Y., J. Yang, Y. Chen, P. De Maeyer, Z. Li & W. Duan (2018) Detecting the Causal Effect of Soil Moisture on Precipitation Using Convergent Cross Mapping. *Scientific Reports,* 8**,** 12171.

Wang, Z. P. & X. G. Han (2005) Diurnal variation in methane emissions in relation to plants and environmental variables in the Inner Mongolia marshes. *Atmospheric Environment,* 39**,** 6295-6305.

Ward, N. D., J. P. Megonigal, B. Bond-Lamberty, V. L. Bailey, D. Butman, E. A. Canuel, H. Diefenderfer, N. K. Ganju, M. A. Goñi, E. B. Graham, C. S. Hopkinson, T. Khangaonkar, J. A. Langley, N. G. McDowell, A. N. Myers-Pigg, R. B. Neumann, C. L. Osburn, R. M. Price, J. Rowland, A. Sengupta, M. Simard, P. E. Thornton, M. Tzortziou, R. Vargas, P. B. Weisenhorn & L. Windham-Myers (2020) Representing the function and sensitivity of coastal interfaces in Earth system models. *Nature Communications,* 11**,** 2458.

Wuebbles, D. J. & K. Hayhoe (2002) Atmospheric methane and global change. *Earth-Science Reviews,* 57**,** 177-210.

Yang, B., X. Li, S. Lin, C. Jiang, L. Xue, J. Wang, X. Liu, M. Espenberg, J. Pärn & Ü. Mander (2021) Invasive Spartina alterniflora changes the Yangtze Estuary salt marsh from CH4 sink to source. *Estuarine, Coastal and Shelf Science,* 252**,** 107258.

Ye, A. Clark, E. Deyle & G. Sugihara (2016) rEDM: an R package for empirical dynamic modeling and convergent cross-mapping. *cran. r-project. org*.

Ye, H., R. J. Beamish, S. M. Glaser, S. C. H. Grant, C.-h. Hsieh, L. J. Richards, J. T. Schnute & G. Sugihara (2015a) Equation-free mechanistic ecosystem forecasting using empirical dynamic modeling. *Proceedings of the National Academy of Sciences,* 112**,** E1569-E1576.

Ye, H., E. R. Deyle, L. J. Gilarranz & G. Sugihara (2015b) Distinguishing time-delayed causal interactions using convergent cross mapping. *Scientific Reports,* 5**,** 14750.

Yuan, J. J., W. X. Ding, D. Y. Liu, H. Kang, J. Xiang & Y. X. Lin (2016) Shifts in methanogen community structure and function across a coastal marsh transect: effects of exotic Spartina alterniflora invasion. *Scientific Reports,* 6.

Yuan, J. J., D. Y. Liu, Y. Ji, J. Xiang, Y. X. Lin, M. Wu & W. X. Ding (2019) Spartina alterniflora invasion drastically increases methane production potential by shifting methanogenesis from hydrogenotrophic to methylotrophic pathway in a coastal marsh. *Journal of Ecology,* 107**,** 2436-2450.

Yvon-Durocher, G., A. P. Allen, D. Bastviken, R. Conrad, C. Gudasz, A. St-Pierre, N. Thanh-Duc & P. A. del Giorgio (2014) Methane fluxes show consistent temperature dependence across microbial to ecosystem scales. *Nature,* 507**,** 488-491.

Zaki, M. T. & O. I. Abdul-Aziz (2022) Predicting greenhouse gas fluxes in coastal salt marshes using artificial neural networks. *Wetlands,* 42.

Zhang, Q., L. Ting-Ting, Q. Zhang, W. Guo-Cheng, Y. Li-Jun, G. Bin & H. Peng-Fei (2020) Accuracy analysis in CH4MODwetland in the simulation of CH4 emissions from Chinese wetlands. *Advances in Climate Change Research,* 11**,** 52-59.

Zhang, Z., N. E. Zimmermann, A. Stenke, X. Li, E. L. Hodson, G. F. Zhu, C. L. Huang & B. Poulter (2017) Emerging role of wetland methane emissions in driving 21st century climate change. *Proceedings of the National Academy of Sciences of the United States of America,* 114**,** 9647-9652.

Zhao, M. L., G. X. Han, J. Y. Li, W. M. Song, W. D. Qu, F. Eller, J. P. Wang & C. S. Jiang (2020) Responses of soil CO2 and CH4 emissions to changing water table level in a coastal wetland. *Journal of Cleaner Production,* 269.

Zhu, X. D., L. X. Meng, Y. H. Zhang, Q. H. Weng & J. Morris (2019) Tidal and Meteorological Influences on the Growth of Invasive Spartina alterniflora: Evidence from UAV Remote Sensing. *Remote Sensing,* 11.

Zhu, X. D., Q. L. Zhuang, Z. C. Qin, M. Glagolev & L. L. Song (2013) Estimating wetland methane emissions from the northern high latitudes from 1990 to 2009 using artificial neural networks. *Global Biogeochemical Cycles,* 27**,** 592-604.